$\mathcal{L}_1$ ADAPTIVE CONTROL FOR ENHANCING PERFORMANCE AND ROBUSTNESS IN COOPERATIVE ROTORCRAFT TRANSPORTATION

Elia Costantini[*,a,1], Emanuele L. de Angelis[a,2], Chiara Gabellieri[b,3], Fabrizio Giulietti[a,4]

[a] *University of Bologna, Department of Industrial Engineering (DIN), CIRI Aerospace, Forlì, 47121, Italy*
[b] *University of Twente, Robotics and Mechatronics (RaM) Department, Electrical Engineering, Mathematics, and Computer Science (EEMCS) Faculty, 7500 AE Enschede, The Netherlands*

ABSTRACT

Cooperative suspended-load transportation using multirotor unmanned aerial vehicles is gaining increasing relevance in a variety of applications, including last–mile parcel delivery and rapid deployment in disaster–relief logistics. However, these operations entail significant challenges related to energy efficiency, safety, and public acceptance. This study proposes a cooperative $\mathcal{L}_1$ augmentation scheme integrated with a baseline formation control strategy for a pair of rotorcraft transporting a shared slung payload. By leveraging the dynamic decoupling achieved through a Lagrangian linearization of the cooperative suspended–load system, the proposed control augmentation compensates for both matched and unmatched model uncertainties as well as external disturbances. The efficacy of the method is demonstrated through high–fidelity numerical simulations that replicate suitable urban air mobility and delivery scenarios, incorporating two heavy–lift octarotors subject to environmental disturbances and rotor–induced aerodynamic effects, modeled using Blade Element Theory. Relative to the baseline controller, the augmented approach exhibits improved position and velocity tracking performance, along with decreased energy consumption, thereby contributing to enhanced operational safety.

1. INTRODUCTION

Among the wide concept of Urban Air Mobility (UAM), air delivery operations using Unmanned Aerial Vehicles (UAVs) emerge as a disruptive solution to reduce ground traffic congestion and its environmental impact by exploiting the vertical dimension (Ref. 1). In particular, UAVs stand out for their potential in transporting essential goods and medical equipment or in performing disaster-relief tasks, thanks to their ability to reach restricted areas and provide critical aid in emergency situations (Refs. 2 and 3). In this respect, the floods in Emilia Romagna (Italy) in May 2023 are a case in point: evacuation challenges and transportation delays suggest the need for more efficient aerial solutions to alleviate the ground infrastructure overload (Ref. 4). In addition, unmanned aerial systems show great potential in firefighting, hazardous environment operations, and search–and–rescue missions, where human intervention may be risky. However, these applications require high robustness to unpredictable environmental disturbances that can significantly affect vehicle dynamics, thus creating the need for more advanced and reliable control strategies.

In aerial delivery operations, two primary payload transportation strategies are commonly employed (Ref. 5): direct attachment of the payload to the air vehicle or suspension via a cable. The rigid attachment method, typically implemented using clamps, grippers, or sufficiently large cargo bays, is the most prevalent approach. However, this configuration tends to increase the take–off mass, system cost, and mechanical complexity,

[*]Corresponding author
[1]Ph.D. Student, elia.costantini3@unibo.it
[2]Associate Professor, emanuele.deangelis4@unibo.it
[3]Assistant Professor, c.gabellieri@utwente.nl
[4]Full Professor, fabrizio.giulietti@unibo.it

and may prove impractical for large payloads or in scenarios where landing is infeasible, such as constrained or hazardous environments (Refs. 6 and 8). Alternatively, the suspended–load strategy offers advantages in terms of preserving rotorcraft performance and reducing system complexity, while enabling payload deployment without requiring the vehicle to land. Nevertheless, this method introduces significant challenges: the suspended payload generates additional forces and moments that alter the vehicle's dynamics, increasing sensitivity to external disturbances and complicating control. Furthermore, load oscillations pose a risk of damaging either the payload or nearby structures through unintended collisions. Consequently, the active suppression of payload swing emerges as a critical and challenging aspect in the design and operation of such systems (Refs. 9 and 10).

The $\mathcal{L}_1$ Adaptive Control ($\mathcal{L}_1$ AC), originally introduced in Refs. 11–14, has been successfully applied to various aerospace applications, thanks to its ability to simultaneously ensure robustness to wide–ranging uncertainties, boundedness of internal signals, and fast adaptation capabilities. By enforcing a clear separation between the estimation and the control loops, $\mathcal{L}_1$ control architectures preserve the baseline controller's stability while rapidly compensating for parameter variations, external disturbances, or partial failures. Although this technique has been widely adopted in fixed–wing applications, more recent research has investigated its potential in rotorcraft systems, including helicopters and multirotors (Refs. 15–17). In Ref. 15 an adaptive augmentation system is developed to enhance a helicopter's baseline controller, demonstrating improved robustness in handling uncertainties and nominal parameter variations. Similarly, in Ref. 16, a classical quadrotor geometric controller is augmented by a $\mathcal{L}_1$ AC to cope for convective wind and exogenous uncertainties. The strategy proposed by the authors demonstrates the ability to track a desired trajectory, with the adaptive controller specifically accounting for external disturbances. Another relevant application of $\mathcal{L}_1$ AC in multirotor UAVs is related to wind gust rejection, a critical factor for aerial operations in complex environments. In this respect, the work in Ref. 17 presents an $\mathcal{L}_1$ output feedback velocity controller for quadrotors employed in wind turbine inspection tasks, in the presence of strong and unpredictable disturbances. Simulations and experimental results are provided, demonstrating the effectiveness of the adaptive controller with respect to the baseline one.

Despite these promising advancements, $\mathcal{L}_1$ AC remains largely unexplored in cooperative rotorcraft transportation scenarios, where the coordination of multiple vehicles gives the possibility to carry heavier payloads and accomplish tasks even in case of vehicle failure, increasing safety, allowing to simultaneously satisfy requirements in terms of: (i) formation geometry–keeping, (ii) trajectory–tracking, (iii) payload swing damping, and (iv) robustness to external disturbances and uncertainties for (v) a generic rotary–wing configuration. In this respect, the present work aims at filling this literature gap by proposing a $\mathcal{L}_1$ AC augmentation to the state–feedback controller for cooperative UAV slung–load system developed by the same authors in Ref. 18. First, the equations of motion of the coupled slung–load system are derived according to the Lagrangian approach. The obtained model is based on a set of simplifying assumptions that include the description of the lifting vehicles and the load as point–masses, while cables are assumed to be rigid and mass–less. An ad hoc parametrization of payload position is proposed to characterize the oscillation state, and the complete system is shown to be inherently underactuated. The model is linearized about the hovering condition with the payload at rest and a fully analytical framework to analyze stability and controllability of the cooperative slung–load system is derived. Starting from the results of a recent work by some of the authors (Ref. 19), a baseline controller is introduced for a formation of two agents to perform trajectory–tracking and formation geometry–keeping. The formation controller is supported by an auxiliary contribution based on the proportional feedback of swing angle and rate information, made available by the onboard Inertial Measurement Unit (IMU), thanks to the observation algorithms developed by the authors in Refs. 20–22. By leveraging a $\mathcal{L}_1$ piecewise adaptive constant law on top of this baseline control scheme, the augmented strategy allows to rapidly reject external disturbances and handle both matched and unmatched uncertainties, while maintaining a more energy–efficient formation flight. Moreover, due to the decoupled nature of the forward–swing motion and lateral–vertical dynamics, the adaptive controller is independently tuned to guarantee the best compromise between performance and robustness. The proposed hybrid approach not only outperforms the baseline controller, but also remains computationally efficient and easily integrable into commercial off–the–shelf control solutions (Ref. 23).

The validity of the method and the performance of the controller are evaluated by numerical simulations in a realistic test case, where a formation made of two octarotors is detailed through the description of powerplant components and the blade–element characterization of propellers (Refs. 24–26). Sample air delivery maneuvers are proposed for a non–nominal scenario with visco–elastic cables in the presence of environmental disturbances, model uncertainties, and noisy sensor readings.

2. SYSTEM MODELING

Starting from the definition of reference frames, a three degrees–of–freedom mathematical model is adopted to describe both the rotorcraft and the load. After formulating the control problem, numerical validation is performed by considering the i–th multirotor as a rigid body with center of gravity P_i. The vehicles and the suspension cables are assumed to be identical.

2.1. Reference frames

Three right–handed orthogonal reference frames are introduced:

1. an Earth–fixed North–East–Down frame, $\mathcal{F}_E = \{O_E; \boldsymbol{x}_E, \boldsymbol{y}_E, \boldsymbol{z}_E\}$: the origin, O_E, is fixed to a point on the Earth's surface, $\boldsymbol{x}_E$ aims in the direction of geodetic North, $\boldsymbol{z}_E$ points downward along the Earth ellipsoid normal, and $\boldsymbol{y}_E$ completes a right-handed triad. This frame is assumed to be inertial under the assumption of flat and non–rotating Earth;

2. two Body–fixed frames, $\mathcal{F}_{Bi} = \{P_i; \boldsymbol{x}_{Bi}, \boldsymbol{y}_{Bi}, \boldsymbol{z}_{Bi}\}$, $i = 1, 2$. The longitudinal axis $\boldsymbol{x}_{Bi}$ is positive out the nose of the i–th rotorcraft in its selected plane of symmetry, $\boldsymbol{z}_{Bi}$ aims in the direction of fuselage/frame bottom, and $\boldsymbol{y}_{Bi}$ completes a right–handed triad;

3. a rotorcraft structural reference frame, $\mathcal{F}_S = \{O_S; \boldsymbol{x}_S, \boldsymbol{y}_S, \boldsymbol{z}_S\}$, used to locate the center of gravity and all vehicle components: axes are parallel to the body–fixed frame axes, such that $\boldsymbol{x}_S = -\boldsymbol{x}_B$, $\boldsymbol{y}_S = \boldsymbol{y}_B$, and $\boldsymbol{z}_S = -\boldsymbol{z}_B$. Stationlines ($ST$) are measured positive aft along the longitudinal axis. Buttlines (BL) are lateral distances, positive to the right, and waterlines (WL) are measured vertically, positive upward. Without loss of generality, it is assumed that O_S lies on the top surface of multirotor frame and is aligned vertically with multirotor geometric center over the $\boldsymbol{x}_S - \boldsymbol{y}_S$ plane.

A sketch of the i–th rotorcraft including the selected reference frames is reported in Fig. 1.

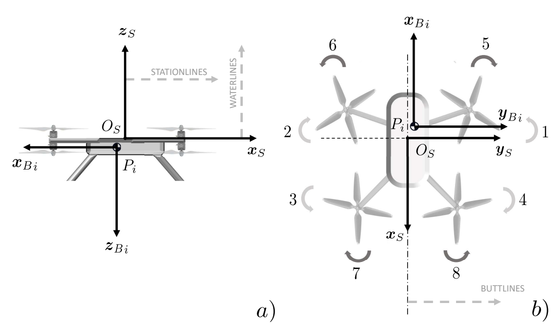

Figure 1: Multirotor body–fixed reference frames.

Vector transformation between $\mathcal{F}_E$ and $\mathcal{F}_{Bi}$ is provided by the rotation matrix $\boldsymbol{T}_{BE}(\boldsymbol{\alpha}_i)$, where $\boldsymbol{\alpha}_i = [\phi_i,\, \theta_i,\, \psi_i]^T$ describes the attitude of the i–th rotorcraft through the classical 'roll', 'pitch', and 'yaw' angles, defined by a ZYX Tait–Bryan extrinsic rotation sequence (Refs. 10 and 27). The following notation is adopted: if $\boldsymbol{w}$ is an arbitrary vector, its components are transformed from $\mathcal{F}_E$ to $\mathcal{F}_{Bi}$ through $\boldsymbol{w}_{Bi} = \boldsymbol{T}_{BE}(\boldsymbol{\alpha}_i)\, \boldsymbol{w}_E$. In what follows, the subscript E is dropped for simplicity.

2.2. Equations of motion

Let $\boldsymbol{r}_i = [r_{xi},\, r_{y_i},\, r_{zi}]^T$ be the position of the i–th agent and $\boldsymbol{v}_i = [v_{xi},\, v_{y_i},\, v_{zi}]^T$ its velocity with respect to the inertial frame. A suspended load with mass m_l is connected in P_l by a cable to the i–th rotorcraft. The dynamics of each agent as expressed in $\mathcal{F}_E$ is described by the following equations:

$$\dot{\boldsymbol{r}}_i = \boldsymbol{v}_i \tag{1}$$

$$\dot{\boldsymbol{v}}_i = \frac{1}{m}\big(m\,\boldsymbol{g} + \boldsymbol{f}_{li} + \boldsymbol{f}_{di} + \boldsymbol{f}_{ci}\big) \tag{2}$$

where m is mass of the rotorcraft, $\boldsymbol{g} = [0,\, 0,\, g]^T$ is local gravitational acceleration vector, $\boldsymbol{f}_{li} = [f_{xl_i},\, f_{y_{l_i}},\, f_{zl_i}]^T$ is the force induced by the load on the i–th rotorcraft through the cable, and $\boldsymbol{f}_{di} = [f_{xd_i},\, f_{y_{d_i}},\, f_{zd_i}]^T$ is vehicle aerodynamic disturbance, that accounts for the contributions of rotorcraft frame drag and rotor in–plane forces. The thrust vector $\boldsymbol{f}_{ci} = [f_{xc_i},\, f_{y_{c_i}},\, f_{zc_i}]^T$, directed along $\boldsymbol{z}_{Bi}$ and pointing upwards, represents the only control input to Eq. (2). It is assumed that the i–th cable is connected to the center of gravity of the i–th agent, such that $\boldsymbol{f}_{li}$ has no effect on attitude motion. Each cable is modeled as mass–less and rigid with constant nominal length L.

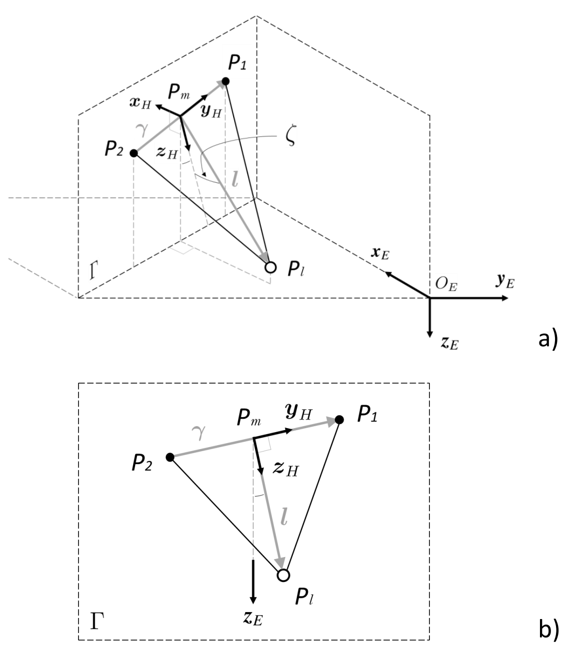

Figure 2: Definition of oscillation angle ζ.

With respect to payload position $\boldsymbol{r}_l = [r_{xl},\, r_{y_l},\, r_{zl}]^T$, an ad hoc parametrization is adopted which stems from the approach in Ref. 20. Let P_m be the midpoint between P_1 and P_2, with position $\boldsymbol{r}_m = (\boldsymbol{r}_1 + \boldsymbol{r}_2)/2$ (see Fig. 2.a). Define $\boldsymbol{\gamma} = \boldsymbol{r}_1 - \boldsymbol{r}_2$ and $\boldsymbol{\beta} = (\boldsymbol{\gamma}/\gamma) \times \boldsymbol{z}_E$, where $\gamma = \|\boldsymbol{\gamma}\|$ and '$\times$' is the cross–product operator. Consider the reference frame $\mathcal{F}_H = \{P_m; \boldsymbol{x}_H, \boldsymbol{y}_H, \boldsymbol{z}_H\}$ with axes $\boldsymbol{x}_H = \boldsymbol{\beta}/\beta$, $\boldsymbol{y}_H = \boldsymbol{\gamma}/\gamma$, and $\boldsymbol{z}_H = \boldsymbol{x}_H \times \boldsymbol{y}_H = (\boldsymbol{\beta}/\beta) \times (\boldsymbol{\gamma}/\gamma)$, provided $\beta = \|\boldsymbol{\beta}\|$. Note that $\boldsymbol{y}_H$ and $\boldsymbol{z}_H$ lie on the local vertical plane Γ that contains the vehicles, while $\boldsymbol{x}_H$ identifies the plane's normal direction as in Fig. 2.b.

Vector transformation between $\mathcal{F}_H$ and $\mathcal{F}_E$ is provided by rotation matrix $\boldsymbol{T}_{EH} = [\boldsymbol{x}_H \quad \boldsymbol{y}_H \quad \boldsymbol{z}_H]$, where unit vector components are expressed in $\mathcal{F}_E$ as:

$$\boldsymbol{x}_H = \big[r_{y_1} - r_{y_2},\, r_{x2} - r_{x1},\, 0\big]^T/\beta \tag{3}$$

$$\boldsymbol{y}_H = \big[r_{x1} - r_{x2},\, r_{y_1} - r_{y_2},\, r_{z1} - r_{z2}\big]^T/\gamma \tag{4}$$

$$\begin{aligned}\boldsymbol{z}_H = \big[&-\big(r_{x1} - r_{x2}\big)\big(r_{z1} - r_{z2}\big),\\ &-\big(r_{y_1} - r_{y_2}\big)\big(r_{z1} - r_{z2}\big),\\ &\big(r_{x1} - r_{x2}\big)^2 + \big(r_{y_1} - r_{y_2}\big)^2\big]^T/(\beta\,\gamma)\end{aligned} \tag{5}$$

with

$$\beta = \sqrt{\big(r_{x1} - r_{x2}\big)^2 + \big(r_{y_1} - r_{y_2}\big)^2} \tag{6}$$

$$\gamma = \sqrt{\big(r_{x1} - r_{x2}\big)^2 + \big(r_{y_1} - r_{y_2}\big)^2 + \big(r_{z1} - r_{z2}\big)^2} \tag{7}$$

Let $\hat{\boldsymbol{l}} = \boldsymbol{l}/\,\|\boldsymbol{l}\|$ be the unit vector directed from P_m to P_l, where $\boldsymbol{l} = \boldsymbol{r}_l - \boldsymbol{r}_m$ and $\|\boldsymbol{l}\| = \sqrt{L^2 - \gamma^2/4}$ is obtained from simple geometric considerations. Payload position is parametrized through the angle $-\pi/2 < \zeta < \pi/2$, obtained from load rotation about $\boldsymbol{y}_H$. Let $\hat{\boldsymbol{l}} = \boldsymbol{T}_{EH}\,\hat{\boldsymbol{l}}_H$ and consider $\hat{\boldsymbol{l}}_H = [\sin\zeta,\, 0,\, \cos\zeta]^T$. Payload position is calculated as a function of ζ, $\boldsymbol{r}_1$, and $\boldsymbol{r}_2$ as follows:

$$\begin{aligned}\boldsymbol{r}_l &= \boldsymbol{r}_m + \|\boldsymbol{l}\|\;\boldsymbol{T}_{EH}\,[\sin\zeta,\, 0,\, \cos\zeta]^T\\ &= \big(\boldsymbol{r}_1 + \boldsymbol{r}_2\big)/2\\ &\quad + \big(\sqrt{L^2 - \gamma^2/4}\big)\,\boldsymbol{T}_{EH}\,[\sin\zeta,\, 0,\, \cos\zeta]^T\end{aligned} \tag{8}$$

Let $\boldsymbol{\lambda} = [\boldsymbol{r}_1^T,\, \boldsymbol{r}_2^T,\, \zeta]^T \in \mathbb{R}^7$ be a vector of generalized coordinates. The Lagrangian equation with respect to $\boldsymbol{\lambda}$ is:

$$\frac{d}{dt}\left(\frac{\partial E}{\partial \dot{\boldsymbol{\lambda}}}\right) - \frac{\partial E}{\partial \boldsymbol{\lambda}} = \boldsymbol{\tau} \tag{9}$$

where $E = K - U$ is the Lagrangian function and $\boldsymbol{\tau} \in \mathbb{R}^7$ is the vector of generalized forces. K is system kinetic energy, given by

$$K = \frac{1}{2}\, m \left(\dot{\boldsymbol{r}}_1^T \dot{\boldsymbol{r}}_1 + \dot{\boldsymbol{r}}_2^T \dot{\boldsymbol{r}}_2\right) + \frac{1}{2}\, m_l\, \dot{\boldsymbol{r}}_l^T \dot{\boldsymbol{r}}_l \tag{10}$$

where $\dot{\boldsymbol{r}}_l$ denotes load velocity as obtained from Eq. (8), namely:

$$\begin{aligned}\dot{\boldsymbol{r}}_l &= \left(\dot{\boldsymbol{r}}_1 + \dot{\boldsymbol{r}}_2\right)/2 \\ &\quad - \frac{\gamma\, \dot{\gamma}}{2\sqrt{4\,L^2 - \gamma^2}}\, \boldsymbol{T}_{EH}\, [\sin\zeta,\, 0,\, \cos\zeta]^T \\ &\quad + \left(\sqrt{L^2 - \gamma^2/4}\right) \Big\{ \dot{\boldsymbol{T}}_{EH}\, [\sin\zeta,\, 0,\, \cos\zeta]^T \\ &\quad + \boldsymbol{T}_{EH}\, [\cos\zeta,\, 0,\, -\sin\zeta]^T\, \dot{\zeta} \Big\}\end{aligned} \tag{11}$$

With respect to time–derivatives $\dot{\boldsymbol{T}}_{EH}$ and $\dot{\gamma}$ in Eq. (11), it is $\dot{\boldsymbol{T}}_{EH} = [\dot{\boldsymbol{x}}_H \quad \dot{\boldsymbol{y}}_H \quad \dot{\boldsymbol{z}}_H]$, where:

$$\dot{\boldsymbol{x}}_H = \left(\dot{\boldsymbol{\beta}}\, \beta - \boldsymbol{\beta}\, \dot{\beta}\right)/\beta^2 \tag{12}$$

$$\dot{\boldsymbol{y}}_H = \left(\dot{\boldsymbol{\gamma}}\, \gamma - \boldsymbol{\gamma}\, \dot{\gamma}\right)/\gamma^2 \tag{13}$$

$$\begin{aligned}\dot{\boldsymbol{z}}_H &= \left[\left(\dot{\boldsymbol{\beta}}\, \beta - \boldsymbol{\beta}\, \dot{\beta}\right)/\beta^2\right] \times \left(\boldsymbol{\gamma}/\gamma\right) \\ &\quad + \left[\left(\dot{\boldsymbol{\gamma}}\, \gamma - \boldsymbol{\gamma}\, \dot{\gamma}\right)/\gamma^2\right] \times \left(\boldsymbol{\beta}/\beta\right)\end{aligned} \tag{14}$$

while

$$\dot{\boldsymbol{\beta}} = \left[\dot{r}_{y_1} - \dot{r}_{y_2},\, \dot{r}_{x_2} - \dot{r}_{x_1},\, 0\right]^T \tag{15}$$

$$\begin{aligned}\dot{\beta} &= \left[\left(\dot{r}_{x_1} - \dot{r}_{x_2}\right)\left(r_{x1} - r_{x2}\right) \right.\\ &\quad \left. + \left(\dot{r}_{y_1} - \dot{r}_{y_2}\right)\left(r_{y1} - r_{y2}\right)\right]/\beta\end{aligned} \tag{16}$$

$$\dot{\boldsymbol{\gamma}} = \left[\dot{r}_{x_1} - \dot{r}_{x_2},\, \dot{r}_{y_1} - \dot{r}_{y_2},\, \dot{r}_{z_1} - \dot{r}_{z_2}\right]^T \tag{17}$$

$$\begin{aligned}\dot{\gamma} &= \left[\left(\dot{r}_{x_1} - \dot{r}_{x_2}\right)\left(r_{x1} - r_{x2}\right) \right.\\ &\quad + \left(\dot{r}_{y_1} - \dot{r}_{y_2}\right)\left(r_{y1} - r_{y2}\right) \\ &\quad \left. + \left(\dot{r}_{z_1} - \dot{r}_{z_2}\right)\left(r_{z1} - r_{z2}\right)\right]/\gamma\end{aligned} \tag{18}$$

Potential energy U is related to the vertical displacement of the agents and the suspended load:

$$U = -m\, g\left(r_{z1} + r_{z2}\right) - m_l\, g\, r_{zl} \tag{19}$$

Given the energy contributions in Eqs. (10) and (19) and taking into account the state of the load as described by Eqs. (8) and (11), the Lagrangian equation is manipulated into the system:

$$\dot{\boldsymbol{\lambda}} = \boldsymbol{\mu} \tag{20}$$

$$\boldsymbol{M}(\boldsymbol{\lambda})\, \dot{\boldsymbol{\mu}} + \boldsymbol{C}(\boldsymbol{\lambda}, \boldsymbol{\mu})\, \boldsymbol{\mu} + \boldsymbol{G}(\boldsymbol{\lambda}) = \boldsymbol{\tau} \tag{21}$$

where $\boldsymbol{\mu} = [\boldsymbol{v}_1^T,\, \boldsymbol{v}_2^T,\, \dot{\zeta}]^T \in \mathbb{R}^7$. For the sake of brevity the highly–nonlinear and lengthy expressions of terms $\boldsymbol{M}(\boldsymbol{\lambda})$, $\boldsymbol{C}(\boldsymbol{\lambda}, \boldsymbol{\mu})$, and $\boldsymbol{G}(\boldsymbol{\lambda})$ are not detailed in the present framework but can be made available to the reader upon request. The generalized force vector $\boldsymbol{\tau} = \boldsymbol{\tau}_c + \boldsymbol{\tau}_d \in \mathbb{R}^7$ is made of a control contribution, $\boldsymbol{\tau}_c$, and a disturbance term, $\boldsymbol{\tau}_d$, that mostly accounts for the aerodynamic drag effects. In particular, it is $\boldsymbol{\tau}_c = [\boldsymbol{f}_{c1}^{\,T},\, \boldsymbol{f}_{c2}^{\,T},\, 0]^T$ and $\boldsymbol{\tau}_d = [\boldsymbol{f}_{d1}^{\,T},\, \boldsymbol{f}_{d2}^{\,T},\, 0]^T - \boldsymbol{D}\, \boldsymbol{\mu}$, where the latter term accounts for payload drag at low oscillation speed, provided $\boldsymbol{D} = \mathrm{diag}(0,\, 0,\, 0,\, 0,\, 0,\, 0,\, d) \in \mathbb{R}^{7\times 7}$ and $d > 0$ is a drag coefficient.

Remark 1. The constraint on the definition of oscillation angle ζ is considered to avoid singularities in the proposed mathematical representation. In fact, $\boldsymbol{M}(\boldsymbol{\lambda})$ becomes singular if $\zeta = \pm\,\pi/2$ rad, which occurs when $\hat{\boldsymbol{l}}$ aims in the direction of $\boldsymbol{x}_H$. However, such situation is unlikely to be encountered in practice, provided that aggressive maneuvers or unusual attitudes are not envisaged in safe delivery operations.

3. CONTROL SYSTEM DESIGN

3.1. System linearization

Let $\bar{\boldsymbol{\gamma}} = [\bar{\gamma}_x,\, \bar{\gamma}_y,\, 0]^T$ be the prescribed mutual distance vector between the two agents of the formation, with components expressed in $\mathcal{F}_E$, such that $\bar{\gamma} = \sqrt{\bar{\gamma}_x^2 + \bar{\gamma}_y^2} < 2\,L$. The system in Eqs. (20) and (21) is linearized about the equilibrium $(\bar{\boldsymbol{x}},\, \bar{\boldsymbol{u}})$, where $\bar{\boldsymbol{x}} = [\bar{\boldsymbol{\lambda}}^T,\, \bar{\boldsymbol{\mu}}^T]^T = [\boldsymbol{r}_1^T,\, (\boldsymbol{r}_1 - \bar{\boldsymbol{\gamma}})^T,\, \boldsymbol{0}_{1\times 8}]^T \in \mathbb{R}^{14}$ describes a hovering flight where the three point–masses lie on the local vertical plane Γ (see Fig. 2). The term $\bar{\boldsymbol{u}} = [\bar{\boldsymbol{u}}_1^T,\, \bar{\boldsymbol{u}}_2^T]^T \in \mathbb{R}^6$ represents the proper equilibrium force, where $\bar{\boldsymbol{u}}_1 = \bar{\boldsymbol{f}}_{c_1} + \bar{\boldsymbol{f}}_{d_1}$ and $\bar{\boldsymbol{u}}_2 = \bar{\boldsymbol{f}}_{c_2} + \bar{\boldsymbol{f}}_{d_2}$. In such a condition, Agent 2 is required to maintain the prescribed position $\bar{\boldsymbol{r}}_2 = \boldsymbol{r}_1 - \bar{\boldsymbol{\gamma}}$, while the suspended load is at rest, namely $\bar{\zeta} = \dot{\bar{\zeta}} = 0$. The generalized equilibrium force is obtained as $\bar{\boldsymbol{\tau}} = \bar{\boldsymbol{\tau}}_c + \bar{\boldsymbol{\tau}}_d = \boldsymbol{G}(\bar{\lambda})$. Let $M = 2\,m + m_l$ be the total system mass and define $\xi_i = 2\,(1 - i) + 1$. Taking into account the first six components in $\bar{\boldsymbol{\tau}}$, the proper equilibrium force $\bar{\boldsymbol{u}}_i$ results to be

$$\bar{\boldsymbol{u}}_i = \left[\frac{g\, m_l\, \xi_i\, \bar{\gamma}_x}{2\sqrt{4\, L^2 - \bar{\gamma}^2}},\ \frac{g\, m_l\, \xi_i\, \bar{\gamma}_y}{2\sqrt{4\, L^2 - \bar{\gamma}^2}},\ -\frac{g\, M}{2}\right]^T. \tag{22}$$

Let $\boldsymbol{x} = [\boldsymbol{\lambda}^T,\, \boldsymbol{\mu}^T]^T \in \mathbb{R}^{14}$ and $\boldsymbol{u} = [\boldsymbol{u}_1^T,\, \boldsymbol{u}_2^T]^T \in \mathbb{R}^6$ be the state and input vectors respectively describing the dynamics in Eq. (20) and (21), linearized about the considered equilibrium condition. The standard state–space representation $\dot{\boldsymbol{x}} = \tilde{\boldsymbol{A}}\, \boldsymbol{x} + \tilde{\boldsymbol{B}}\, \boldsymbol{u}$ is derived where $\tilde{\boldsymbol{A}} \in \mathbb{R}^{14\times 14}$ is the state matrix and $\tilde{\boldsymbol{B}} \in \mathbb{R}^{14\times 6}$ is the input matrix, according to the detailed expressions in Ref. 18. Define the permutation $\boldsymbol{z} = \mathcal{P}\, \boldsymbol{x}$, where $\boldsymbol{z} \in \mathbb{R}^{14}$ is the re-arranged state vector,

$$\begin{aligned} \boldsymbol{z} = [&r_{x1}, v_{x1},\, r_{x2},\, v_{x2},\, \zeta,\, \dot{\zeta}, \\ &r_{y1},\, v_{y1},\, r_{y2},\, v_{y2}\, r_{z1},\, v_{z1},\, r_{z2},\, v_{z2}]^T \end{aligned} \tag{23}$$

and $\mathcal{P} \in \mathbb{R}^{14\times 14}$ is the transformation map:

$$\begin{aligned} \mathcal{P} = [&\boldsymbol{e}_1,\, \boldsymbol{e}_8, \boldsymbol{e}_4,\, \boldsymbol{e}_{11},\, \boldsymbol{e}_7,\, \boldsymbol{e}_{14}, \\ &\boldsymbol{e}_2,\, \boldsymbol{e}_9,\, \boldsymbol{e}_5,\, \boldsymbol{e}_{12},\, \boldsymbol{e}_3,\, \boldsymbol{e}_{10},\, \boldsymbol{e}_6,\, \boldsymbol{e}_{13}]^T \end{aligned} \tag{24}$$

where $\boldsymbol{e}_k$ is the k–th canonical vector of $\mathbb{R}^{14}$. Since $\mathcal{P}$ is orthogonal (i.e. $\mathcal{P}^{-1} = \mathcal{P}^T$), the transformed model reads

$$\dot{\boldsymbol{z}} = \boldsymbol{A}\, \boldsymbol{z} + \boldsymbol{B}\, \boldsymbol{u}, \qquad \boldsymbol{A} = \mathcal{P}\, \tilde{\boldsymbol{A}}\, \mathcal{P}^T,\ \boldsymbol{B} = \mathcal{P}\, \tilde{\boldsymbol{B}} \tag{25}$$

Without loss of generality, consider the equilibrium $\bar{\gamma}_x = 0$ and $\bar{\gamma}_y = \bar{\gamma}$ for a prescribed $\bar{\gamma}$. $\boldsymbol{A}$ assumes the following block–diagonal formulation

$$\boldsymbol{A} = \begin{bmatrix} \boldsymbol{A}_{fs} & \boldsymbol{0}_{6\times 8} \\ \boldsymbol{0}_{8\times 6} & \boldsymbol{A}_{lv} \end{bmatrix}, \tag{26}$$

where $\boldsymbol{A}_{fs} \in \mathbb{R}^{6\times 6}$ is the subsystem matrix that describes the coupling between the vehicles' forward motion (along $\boldsymbol{x}_H$) and the payload swing, while $\boldsymbol{A}_{lv} \in \mathbb{R}^{8\times 8}$ accounts for the lateral and vertical dynamics of the formation (along $\boldsymbol{y}_H$ and $\boldsymbol{z}_H$, respectively).

3.2. Baseline controller design

The baseline control system is designed to achieve simultaneous (i) formation–keeping, (ii) trajectory–tracking, and optional (iii) payload stabilization. With respect to formation control, let P_r be the reference point identified by position vector $\boldsymbol{r}_r$ and moving with velocity $\boldsymbol{v}_r$, and let D_i be the i–th vehicle's required position, identified by $\bar{\boldsymbol{r}}_i$. One has $\boldsymbol{r}_r + \boldsymbol{d}_i = \boldsymbol{r}_i$ and $\boldsymbol{r}_r + \bar{\boldsymbol{d}}_i = \bar{\boldsymbol{r}}_i$, where $\boldsymbol{d}_i = [d_{xi},\, d_{y_i},\, d_{zi}]^T$ and $\bar{\boldsymbol{d}}_i = [\bar{d}_{x_i},\, \bar{d}_{y_i},\, \bar{d}_{z_i}]^T$ indicate the current and required relative positions between the i-th agent and the reference point, respectively (see Fig. 3).

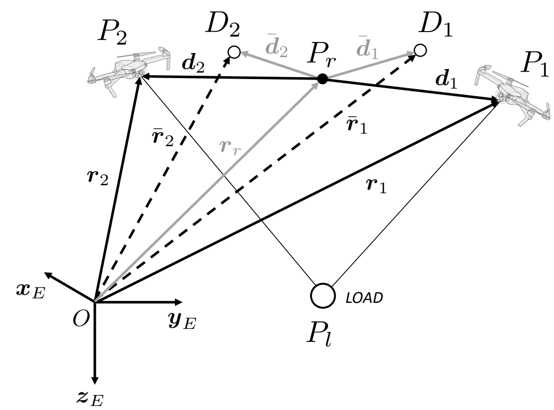

Figure 3: Definition of current (P_i) and desired (D_i) positions of the i-th agent.

Define $\boldsymbol{\delta}_i = [\delta_{xi},\, \delta_{y_i},\, \delta_{zi}]^T = \bar{\boldsymbol{d}}_i - \boldsymbol{d}_i$ and $\boldsymbol{\epsilon}_i = [\epsilon_{xi},\, \epsilon_{y_i},\, \epsilon_{zi}]^T = \boldsymbol{v}_r - \boldsymbol{v}_i$ as the relative position and trajectory error variables, such that $\dot{\boldsymbol{\delta}}_i = \boldsymbol{\epsilon}_i$. Stemming from the idea in Ref. 19, the Formation Controller (FC), adapted to the present framework, is

$$\boldsymbol{u}_i^{(FC)} = \bar{\boldsymbol{u}}_i + m\left(\boldsymbol{K}_\delta\, \boldsymbol{\delta}_i + \boldsymbol{K}_\epsilon\, \boldsymbol{\epsilon}_i\right) \tag{27}$$

where $\bar{\boldsymbol{u}}_i$, $i = 1, 2$, is the trim contribution reported in Eq. (22), while $\boldsymbol{K}_\delta = \mathrm{diag}(K_{\delta_x},\, K_{\delta_y},\, K_{\delta_z})$ and $\boldsymbol{K}_\epsilon = \mathrm{diag}(K_{\epsilon_x},\, K_{\epsilon_y},\, K_{\epsilon_z})$ are positive gain matrices. It is assumed that when the i–th agent reaches the desired position D_i (namely $\boldsymbol{\delta}_i = \boldsymbol{0}_{3\times 1}$, $\boldsymbol{\epsilon}_i = \boldsymbol{0}_{3\times 1}$, $i = 1, 2$), the formation midpoint P_m exactly tracks P_r, leading to $\bar{\boldsymbol{d}}_1 = -\bar{\boldsymbol{d}}_2 = [\bar{\gamma}_x/2,\, \bar{\gamma}_y/2,\, 0]^T$.

The proposed Load Controller (LC) is

$$\boldsymbol{u}_1^{(LC)} = \boldsymbol{u}_2^{(LC)} = m\left(k_p\, \zeta + k_d\, \dot{\zeta}\right) \boldsymbol{x}_H, \tag{28}$$

where k_p and k_d are positive gains. The proportional contribution in Eq. (28) allows the formation to track the payload position over the local horizontal plane along $\boldsymbol{x}_H$, while the derivative contribution damps the motion of the relative position vector $\boldsymbol{l}$ with respect to $\mathcal{F}_H$. Finally, the desired baseline–acceleration for the i–th multirotor is given by

$$\boldsymbol{a}_{sp_i} = [a_{sp_{x\,i}},\, a_{sp_{y\,i}},\, a_{sp_{z\,i}}]^T = \boldsymbol{a}_{sp_i}^{(FC)} + \boldsymbol{a}_{sp_i}^{(LC)} \tag{29}$$

where $\boldsymbol{a}_{sp_i}^{(FC)} = \boldsymbol{u}_{sp_i}^{(FC)}/m$ and $\boldsymbol{a}_{sp_i}^{(LC)} = \boldsymbol{u}_{sp_i}^{(LC)}/m$ are computed using Eqs. (27) and (28), respectively. The stability of the linearized system under the control action in Eqs. (27) and (28) is addressed in the case when $\boldsymbol{v}_r = [0,\,0,\,0]^T$, such that $\dot{\boldsymbol{v}}_r = [0,\,0,\,0]^T$ and $\boldsymbol{r}_r$ is a constant. Let $\boldsymbol{e} = \boldsymbol{z} - \boldsymbol{z}_d = \mathcal{P}\,(\boldsymbol{x} - \boldsymbol{x}_d)$ be the coordinate–transformed error with respect to the desired state $\boldsymbol{x}_d = [\bar{\boldsymbol{r}}_1^T,\, \bar{\boldsymbol{r}}_2^T,\, \boldsymbol{0}_{1\times 8}]^T$. The error dynamics is obtained from Eq. (25) as

$$\dot{\boldsymbol{e}} = \boldsymbol{A}\,\boldsymbol{e} + \boldsymbol{B}\,\boldsymbol{u} \tag{30}$$

By manipulating Eqs. (27) and (28) in the linear framework, one obtains $\boldsymbol{u} = -\boldsymbol{K}_z\,\boldsymbol{e}$, where $\boldsymbol{K}_z = \boldsymbol{K}\,\mathcal{P}^T$ and $\boldsymbol{K} \in \mathbb{R}^{6\times 14}$. The feedback-controlled system evolves according to $\dot{\boldsymbol{e}} = \boldsymbol{A}_m\,\boldsymbol{e}$, where

$$\boldsymbol{A}_m = \boldsymbol{A} - \boldsymbol{B}\,\boldsymbol{K}\,\mathcal{P}^T \tag{31}$$

and

$$\boldsymbol{K} = m \begin{bmatrix} \boldsymbol{K}_\delta & \boldsymbol{0}_{3\times 3} & k_p\,\bar{\boldsymbol{\gamma}} & \boldsymbol{K}_\epsilon & \boldsymbol{0}_{3\times 3} & k_d\,\bar{\boldsymbol{\gamma}} \\ \boldsymbol{0}_{3\times 3} & \boldsymbol{K}_\delta & k_p\,\bar{\boldsymbol{\gamma}} & \boldsymbol{0}_{3\times 3} & \boldsymbol{K}_\epsilon & k_d\,\bar{\boldsymbol{\gamma}} \end{bmatrix}. \tag{32}$$

Remark 2. Since $\mathcal{P}$ is an orthogonal transformation, the state matrix $\boldsymbol{A}_m$ inherits the block–diagonal, decoupled structure of $\boldsymbol{A}$ reported in Eq. (26). The proposed state–feedback, for a given set of control gains, places the eigenvalues of $\boldsymbol{A}_m$ in the open left half–plane, making this matrix Hurwitz (Ref. 18). Thus, the baseline system is exponentially stable and provides the reference model to be augmented by the $\mathcal{L}_1$ adaptive layer discussed in what follows.

3.3. $\mathcal{L}_1$ AC design

A $\mathcal{L}_1$ Piecewise–Constant Adaptive Law (which stems from the idea in Ref. 28) is designed on top of the baseline controller presented in Section 3.2. This augmented control methodology allows to simultaneously (i) maintain formation geometry, (ii) track the desired trajectory, (iii) optionally damp payload swing, and (iv) preserve robustness to external disturbances and both matched and unmatched uncertainties. Exploiting the decoupled nature of the problem, first introduced in Eq. (26), the control system is independently developed for the forward–swing and lateral–vertical channels. In what follows, without loss of generality, only the control architecture implemented for the former dynamics is presented in detail.

Consider the forward–swing system dynamics

$$\begin{aligned} \dot{\boldsymbol{x}}_{fs} &= \boldsymbol{A}_{m_{fs}}\boldsymbol{x}_{fs} + \boldsymbol{B}_{m_{fs}}\left(\boldsymbol{\omega}_{fs}\,\boldsymbol{u}_{fs} + \boldsymbol{f}_{1_{fs}}\right) \\ &\qquad + \boldsymbol{B}_{um_{fs}}\boldsymbol{f}_{2_{fs}}, \qquad \boldsymbol{x}_{fs}(0) = \boldsymbol{x}_{fs_0} \\ \boldsymbol{y}_{fs} &= \boldsymbol{C}_{m_{fs}}\,\boldsymbol{x}_{fs} \end{aligned} \tag{33}$$

where $\boldsymbol{x}_{fs} = \left[r_{x_1},\, v_{x_1},\, r_{x_2},\, v_{x_2},\, \zeta,\, \dot{\zeta}\right]^T \in \mathbb{R}^6$ is the state vector, $\boldsymbol{u}_{fs} = [u_{x_1},\, u_{x_2}]^T \in \mathbb{R}^2$ is the control input, $\boldsymbol{y}_{fs} = [r_{x_1},\, r_{x_2}]^T \in \mathbb{R}^2$ is the regulated output, and $\boldsymbol{\omega}_{fs} \in \mathbb{R}^{2\times 2}$ is the uncertain system input gain matrix. $\boldsymbol{A}_{m_{fs}} \in \mathbb{R}^{6\times 6}$ is Hurwitz (see Remark 2) and defines the desired closed–loop dynamics, $\boldsymbol{B}_{m_{fs}} \in \mathbb{R}^{6\times 2}$ is the input matrix, $\boldsymbol{C}_{m_{fs}} \in \mathbb{R}^{2\times 6}$ is a known constant matrix. Note that the pair $\left(\boldsymbol{A}_{m_{fs}}, \boldsymbol{B}_{m_{fs}}\right)$ must be completely controllable, while $\left(\boldsymbol{A}_{m_{fs}}, \boldsymbol{C}_{m_{fs}}\right)$ must be completely observable. $\boldsymbol{B}_{um_{fs}} \in \mathbb{R}^{6\times 4}$ is a constant matrix such that $\boldsymbol{B}_{m_{fs}}^T\,\boldsymbol{B}_{um_{fs}} = \boldsymbol{0}$ and $rank\left(\left[\boldsymbol{B}_{m_{fs}},\, \boldsymbol{B}_{um_{fs}}\right)\right] = 6$ (full). Consider $\boldsymbol{B}_{fs} \triangleq \left[\boldsymbol{B}_{m_{fs}},\, \boldsymbol{B}_{um_{fs}}\right]$ and let $\boldsymbol{f}_{1_{fs}}$ and $\boldsymbol{f}_{2_{fs}}$ be two unknown, bounded, nonlinear functions satisfying

$$\begin{bmatrix} \boldsymbol{f}_{1_{fs}}(\cdot) \\ \boldsymbol{f}_{2_{fs}}(\cdot) \end{bmatrix} = \boldsymbol{B}_{fs}^{-1}\,\boldsymbol{f}_{fs}(\cdot) \tag{34}$$

where $\boldsymbol{f}_{1_{fs}}(\cdot)$ and $\boldsymbol{B}_{um_{fs}}\,\boldsymbol{f}_{2_{fs}}(\cdot)$ respectively account for matched and unmatched uncertainties (Ref. 28).

The $\mathcal{L}_1$ AC implemented in this work exploits a fast estimation scheme based on a piecewise constant law, whose adaptation rate can be directly associated with the sampling rate of the available CPU. The state predictor assumes the form

$$\begin{aligned} \dot{\hat{\boldsymbol{x}}}_{fs} &= \boldsymbol{A}_{m_{fs}}\hat{\boldsymbol{x}}_{fs} + \boldsymbol{B}_{m_{fs}}\left(\boldsymbol{\omega}_{0_{fs}}\,\boldsymbol{u}_{fs} + \hat{\boldsymbol{\sigma}}_{1_{fs}}\right) \\ &\qquad + \boldsymbol{B}_{um_{fs}}\hat{\boldsymbol{\sigma}}_{2_{fs}}, \qquad \hat{\boldsymbol{x}}_{fs}(0) = \boldsymbol{x}_{fs_0} \\ \hat{\boldsymbol{y}}_{fs} &= \boldsymbol{C}_{m_{fs}}\,\hat{\boldsymbol{x}_{fs}} \end{aligned} \tag{35}$$

where $\boldsymbol{\omega}_{0_{fs}}$ is a known, nominal system input gain contained in a compact convex set $\boldsymbol{\Omega} \subset \mathbb{R}^{2\times 2}$, while $\hat{\boldsymbol{\sigma}}_{1_{fs}} \in \mathbb{R}^2$ and $\hat{\boldsymbol{\sigma}}_{2_{fs}} \in \mathbb{R}^4$ are the adaptive estimates. The adaptation laws for $\hat{\boldsymbol{\sigma}}_{1_{fs}}$ and $\hat{\boldsymbol{\sigma}}_{2_{fs}}$ are defined as

$$\begin{bmatrix} \hat{\boldsymbol{\sigma}}_{1_{fs}} \\ \hat{\boldsymbol{\sigma}}_{2_{fs}} \end{bmatrix} = \begin{bmatrix} \hat{\boldsymbol{\sigma}}_{1_{fs}}(k\,T_s) \\ \hat{\boldsymbol{\sigma}}_{2_{fs}}(k\,T_s) \end{bmatrix}, \quad t \in [k\,T_s,\,(k+1)\,T_s] \tag{36}$$

with

$$\begin{bmatrix} \hat{\boldsymbol{\sigma}}_{1_{fs}}(k\,T_s) \\ \hat{\boldsymbol{\sigma}}_{2_{fs}}(k\,T_s) \end{bmatrix} = -\begin{bmatrix} \mathbb{I}_2 & \mathbf{0}_{2\times 4} \\ \mathbf{0}_{4\times 2} & \mathbb{I}_4 \end{bmatrix} \boldsymbol{B}_{fs}^{-1}\,\boldsymbol{\Phi}_{fs}^{-1}(T_s)\,\boldsymbol{\mu}_{fs}(k\,T_s) \tag{37}$$

for $k = 0,\,1,\,2,...$ and given $T_s > 0$ is the adaptation sampling time, directly related to the available CPU characteristics. In this regard, matrix $\boldsymbol{\Phi}_{fs} \in \mathbb{R}^{6\times 6}$ is

$$\boldsymbol{\Phi}(T_s) \triangleq \boldsymbol{A}_{m_{fs}}^{-1}\left(e^{\boldsymbol{A}_{m_{fs}}T_s} - \mathbb{I}_2\right), \tag{38}$$

while $\boldsymbol{\mu}_{fs} \in \mathbb{R}^6$ is

$$\boldsymbol{\mu}_{fs}(k\,T_s) = e^{\boldsymbol{A}_{m_{fs}}T_s}\,\tilde{\boldsymbol{x}}_{fs}(k\,T_s) \tag{39}$$

provided $\tilde{\boldsymbol{x}}_{fs} = \hat{\boldsymbol{x}}_{fs} - \boldsymbol{x}_{fs}$ is the forward–swing estimation error. Finally, the $\mathcal{L}_1$ forward–swing control is modulated by a feedback gain matrix $\boldsymbol{K}_{fs} \in \mathbb{R}^{2\times 2}$ and by a strictly proper transfer matrix $\boldsymbol{D}_{fs}(s) \in \mathbb{R}^{2\times 2}$ that, for any choice of $\boldsymbol{\omega}_{fs}$, gives a strictly proper stable

$$\boldsymbol{C}(s) \triangleq \boldsymbol{\omega}_{fs}\,\boldsymbol{K}_{fs}\,\boldsymbol{D}_{fs}(s)\,(\mathbb{I}_2 + \boldsymbol{\omega}_{fs}\boldsymbol{K}_{fs}\boldsymbol{D}_{fs}(s))^{-1} \tag{40}$$

where $\mathbb{I}_2 \in \mathbb{R}^{2\times 2}$ is the identity matrix related to the forward-swing state dimension. The $\mathcal{L}_1$ control input is defined as

$$\boldsymbol{u}_{fs}(s) = -\boldsymbol{K}_{fs}\,\boldsymbol{D}_{fs}(s)\,\hat{\boldsymbol{\eta}}_{fs}(s) \tag{41}$$

where $\hat{\boldsymbol{\eta}}_{fs}(s)$ is the Laplace transform of

$$\hat{\boldsymbol{\eta}}_{fs}(t) \triangleq \boldsymbol{\omega}_{0_{fs}}\boldsymbol{u}_{fs}(t) + \hat{\boldsymbol{\eta}}_1(t) + \hat{\boldsymbol{\eta}}_{2_m}(t) - \boldsymbol{r}_g(t) \tag{42}$$

with all quantities defined exactly as in Chapter 3.3 of Ref. 28. The augmented acceleration set–point for the cooperative slung–load system is thus given by $\boldsymbol{a}_{sp}^{(\mathcal{L}_1)} = \boldsymbol{u}_{fs}(t)/m$, where $\boldsymbol{u}_{fs}(t)$ is derived from the Laplace transform of Eq. (41). Finally, a sketch of the overall control system architecture for the i–th multirotor is reported in Fig. 4. Rather than sending commands at the usual position or velocity outer–loops, the proposed controller step in one layer deeper feeding an acceleration set–point. Concerning the $\mathcal{L}_1$ additive contribution, it is implemented only on–board the i–th multirotor, but it is capable of generating the control input for the j–th vehicle as well, significantly reducing the overall computational demand.

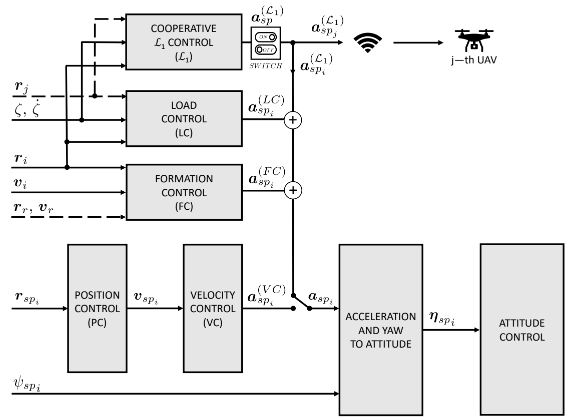

Figure 4: The i–th multirotor control scheme based on PX4 autopilot architecture (Ref. 23).

Remark 3. The $\mathcal{L}_1$ AC layer for the forward–swing dynamics relies on the reduced–state $\boldsymbol{x}_{fs} = \left[r_{x_1},\, v_{x_1},\, r_{x_2},\, v_{x_2},\, \zeta,\, \dot{\zeta}\right]^T$, which includes both the oscillation angle ζ and rate $\dot{\zeta}$. The estimation of the oscillatory state of the payload in the cooperative scenario is a challenging issue that was recently investigated by some of the authors of the present work in Ref. 22. In particular, a method was derived to estimate the swing angle and rate in cooperative multirotor slung–load applications without the need for any extra sensors, apart from the onboard IMUs. In such a framework, accelerometer readings and dynamic model information were fused through a Fading Gaussian Deterministic (FGD) filter in the presence of model uncertainties and measurement noise.

Without loss of generality, a proof of global exponential ultimate boundedness for the forward-swing subsystem is provided in what follows. The proposed methodology, however, can be straightforwardly extended to the lateral–vertical channel.

Theorem 1 Let $\boldsymbol{A}_{m_{fs}}$ be Hurwitz and let $\boldsymbol{P} = \boldsymbol{P}^T > 0$ be a symmetric, positive–definite matrix that solves the Lyapunov equation $\boldsymbol{A}_{m_{fs}}^T \boldsymbol{P} + \boldsymbol{P}\,\boldsymbol{A}_{m_{fs}} = -\boldsymbol{Q}$ with $\boldsymbol{Q} = \boldsymbol{Q}^T > 0$. Let $\boldsymbol{B}_{fs} := \left[\boldsymbol{B}_{m_{fs}}, \boldsymbol{B}_{um_{fs}}\right] \in \mathbb{R}^{6\times 6}$ be non–singular and $\boldsymbol{B}_{m_{fs}}^T \boldsymbol{B}_{um_{fs}} = \boldsymbol{0}$. Let the non–linear functions $\boldsymbol{f}_{1_{fs}}(t)$ and $\boldsymbol{f}_{2_{fs}}(t)$ be bounded by some known quantities $\boldsymbol{\Delta}_1$ and $\boldsymbol{\Delta}_2$, namely $||\boldsymbol{f}_{1_{fs}}(t)|| \leq \boldsymbol{\Delta}_1$, $||\boldsymbol{f}_{2_{fs}}(t)|| \leq \boldsymbol{\Delta}_2$ for all $t > 0$. Let $\boldsymbol{D}_{fs}$ be strictly proper, stable with DC gain satisfying $||\boldsymbol{\omega}_{fs}\boldsymbol{K}_{fs}\boldsymbol{D}_{fs}(0)\left(\mathbb{I}_6 + \boldsymbol{\omega}_{fs}\boldsymbol{K}_{fs}\boldsymbol{D}_{fs}(0)\right)^{-1}|| < 1$ according to the small-gain inequality theorem (see Ref. 28). Assume $T_s > 0$ is chosen such that $||e^{\boldsymbol{A}_{m_{fs}}T_s}|| \leq 1-\alpha$ with $0 < \alpha < 1$. Consider $\tilde{\boldsymbol{x}}_{fs} = \hat{\boldsymbol{x}}_{fs} - \boldsymbol{x}_{fs}$ and $\tilde{\boldsymbol{\sigma}}_{fs} = \hat{\boldsymbol{\sigma}}_{i_{fs}} - \boldsymbol{f}_{i_{fs}}$ to be the state prediction and parameter estimation errors, respectively. Then, by properly picking an adaptation-gain matrix $\boldsymbol{\Lambda}$ so that $\lambda_{\max}(\boldsymbol{\Lambda})$ satisfies (A.13), the closed-loop forward-swing subsystem is globally exponentially ultimately bounded (GEUB). In particular, there exist constants $\rho \in (0,1)$ and $V_\infty > 0$ for which the Lyapunov candidate function

$$V(t) = \tilde{\boldsymbol{x}}_{fs}^T \boldsymbol{P}\,\tilde{\boldsymbol{x}}_{fs} + \tilde{\boldsymbol{\sigma}}_{fs}^T \boldsymbol{\Lambda}^{-1}\,\tilde{\boldsymbol{\sigma}}_{fs} \tag{43}$$

satisfies, for all $t \geq 0$, the geometric inequality

$$V(t) \leq \rho^{\lfloor t/T_s \rfloor}\, V(0) + V_\infty. \tag{44}$$

Moreover, the tracking error is bounded

$$\|\boldsymbol{e}_{fs}(t)\|_\infty \leq g_e \sqrt{\lambda_{\max}(\boldsymbol{\Lambda})\, V_\infty} \tag{45}$$

where $g_e := \|C(s)\|_{\mathcal{L}_1}$ is the $\mathcal{L}_1$ induced norm of Eq. (40).

Proof. See Appendix A.

4. RESULTS

4.1. Simulation platform

The numerical validation is conducted in Matlab® environment with a 4th–order Runge–Kutta solver frequency of 500 Hz (Ref. 29). The agents of the formation are two identical octarotors modeled as rigid bodies. The modeling thoroughly follows the same approach and nomenclature described in Ref. 30, where the selected platform, characterized by a planar set of contra–rotating propellers, is described in detail. For the sake of brevity, only relevant system parameters are listed in Table B.1. The payload is assumed to be a point mass attached through a hook point H, distinct from rotorcraft center of gravity. The payload is affected by aerodynamic drag, provided $A_l = \pi\, R_l^2$ is the frontal area of an equivalent sphere with radius $R_l = 0.5$ m and drag coefficient $C_{dl} = 0.5$. Air parameters are calculated by the International Standard Atmosphere (ISA) model as a function of altitude (Ref. 31). Local gravitational data are provided by the World Geodetic System 1984 model as a function of vehicle latitude, longitude, and altitude (Ref. 32). Let $\boldsymbol{c}_i = \boldsymbol{r}_l - \boldsymbol{r}_i$ be the vector describing the orientation and length of the i–th cable. The force $\boldsymbol{f}_{l\,i}$ in Eq. (2) is calculated from $\boldsymbol{f}_{l\,i} = \left(K\,\Delta L_i + C\,\dot{\Delta L_i}\right)\hat{\boldsymbol{c}}_i$ where K is the elastic constant, $\Delta L_i = \|\boldsymbol{c}_i\| - L$ and $\dot{\Delta L_i}$ are, respectively, the elastic deformation and its time derivative, and $\hat{\boldsymbol{c}}_i = \boldsymbol{c}_i / \|\boldsymbol{c}_i\|$. With respect to the classical Hookes' model in Ref. 30, cable internal damping is accounted by the coefficient C (see Table B.1). The dynamics of each electric propulsion unit, comprising of an Electronic Speed Controller (ESC) and a brushless motor, are represented by a first–order transfer function with time constant $\tau_{em} = 0.05$ s, capturing both electrical and mechanical nonlinearities. This transfer function maps the commanded rotor angular rate to the actual rate delivered by the motor shaft. Non–ideal sensor behavior is considered in terms of noise, bias, and sensor positioning errors. The on–board computer is located at $STA_{PIX} = BL_{PIX} = 0$ m and $WL_{PIX} = -0.15$ m, with axes aligned with $\mathcal{F}_B$–axes. To simulate the effects of sensor noise, zero–mean Gaussian white noise is added to each Euler angle and angular velocity measurement, with standard deviations $\sigma_\alpha = 0.018$ deg and $\sigma_\omega = 0.095$ deg/s, respectively. The body–fixed accelerometer readings are obtained by adding Gaussian white noise with $\sigma_{acc} = 0.015$ m/s^2 and constant biases $\boldsymbol{a}_{bias_1} = [0.015,\, -0.01,\, 0.002]^T$ m/s^2 and $\boldsymbol{a}_{bias_2} = [-0.004,\, 0.007,\, -0.02]^T$ m/s^2 to the simulated values. Error is also considered for vehicle position and velocity expressed in $\mathcal{F}_E$, provided standard deviations $\sigma_p|_{xy} = 0.074$ m and $\sigma_v|_{xy} = 0.009$ m/s affect the motion over the local–horizontal plane, while $\sigma_p|_z = 0.034$ m and $\sigma_v|_z = 0.005$ m/s characterize the vertical component. The onboard computer operates at a frequency of 100 Hz (sample time $\Delta_t = 0.01$ s).

4.2. Performance indicators

Indicators are defined with the aim to quantitatively assess the performance of $\mathcal{L}_1$ AC system with respect to the baseline controller.

- Maneuver time, t_m. It is the total time required to conclude the considered maneuver. According to the different test cases, it can be defined a priori or based on a stopping criterion. In the latter scenario, the simulation starts at $t = 0$ s and is assumed to be concluded when three conditions are simultaneously satisfied: (i) the position error $e_p = \left\| [\boldsymbol{\delta}_1^T \, \boldsymbol{\delta}_2^T] \right\|$ falls below 0.2 m, (ii) the velocity error $e_v = \left\| [\boldsymbol{\epsilon}_1^T \, \boldsymbol{\epsilon}_2^T] \right\|$ falls below 0.2 m/s, and (iii) the absolute value of ζ remains bounded below 0.5 deg for 5 s.

- Average position and velocity errors, $\boldsymbol{e}_{p_{av}}$ and $\boldsymbol{e}_{v_{av}}$. They are calculated as $\boldsymbol{e}_{p_{av}} = I_{\boldsymbol{e}_{p_{av}}}(t_m)/t_m$ and $\boldsymbol{e}_{v_{av}} = I_{\boldsymbol{e}_{v_{av}}}(t_m)/t_m$ respectively, given the integrals

$$I_{\boldsymbol{e}_{p_{av}}}(t_m) = \int_0^{t_m} |\boldsymbol{e}_p(s)| \, ds \tag{46}$$

$$I_{\boldsymbol{e}_{v_{av}}}(t_m) = \int_0^{t_m} |\boldsymbol{e}_v(s)| \, ds. \tag{47}$$

- Maximum position and velocity error, $\boldsymbol{e}_{p_{max}}$ and $\boldsymbol{e}_{v_{max}}$.

- Total propulsive energy, E_{prop}. It is the mechanical energy delivered by electrical motors to propellers, calculated as

$$E_{prop} = \int_0^{t_m} \sum_{j=1}^{8} P_{sh_j}(s) \, ds \tag{48}$$

  where $P_{sh_j} = Q_j \, \Omega_j$ is the output shaft power generated by the j–th motor, $j = 1, \ldots, 8$, obtained from required torque Q_j and angular rate Ω_j under the assumption of null friction torque. Without loss of generality, E_{prop} is calculated for Agent 1 only.

4.3. Test cases

Consider the formation identified by $\bar{\boldsymbol{\gamma}} = [0,\, 10,\, 0]^T$ m, with components expressed in $\mathcal{F}_E$. It is $\bar{\gamma}_x = 0$ m and $\bar{\gamma}_y = 10$ m, such that $\bar{\boldsymbol{d}}_1 = -\bar{\boldsymbol{d}}_2 = [0,\, 5,\, 0]^T$ m. In the absence of external disturbances, the nominal trim contributions in Eq. (22) are $\bar{\boldsymbol{u}}_1 = [0,\, 173.36,\, -1176.80]^T$ N and $\bar{\boldsymbol{u}}_2 = [0,\, -173.36,\, -1176.80]^T$ N, respectively. With respect to the baseline controller, adopted gains are $\boldsymbol{K}_\delta = \mathrm{diag}(0.25,\, 0.25,\, 0.25)$ 1/s^2, $\boldsymbol{K}_\epsilon = \mathrm{diag}(1.5,\, 1.5,\, 1.5)$ 1/s, $k_p = 0$ 1/s^2, and $k_d = 0$ 1/s. Regarding the most relevant $\mathcal{L}_1$ control parameters, a tuning is performed separately for the forward–swing and lateral–vertical dynamics. For the former, it is $\boldsymbol{\omega}_{0_{fs}} = \mathbb{I}_2$, $\boldsymbol{K}_{fs} = \mathrm{diag}(1.5,\, 1.5)$, and $\boldsymbol{D}_{fs} = \mathrm{diag}(1/(15\, s + 1),\, 1/(15\, s + 1))$. For the latter, it is $\boldsymbol{\omega}_{0_{lv}} = \mathbb{I}_4$, $\boldsymbol{K}_{lv} = \mathrm{diag}(5,\, 5,\, 7.5,\, 7.5)$, and $\boldsymbol{D}_{lv} = \mathrm{diag}(1/(10\, s + 1),\, 1/(10\, s + 1),\, 1/(15\, s + 1),\, 1/(15\, s + 1))$.

4.3.1. Test case 1

The UAVs are characterized by the initial state $\boldsymbol{r}_1(0) = [0,\, 5,\, -20]^T$ m, $\boldsymbol{r}_2(0) = [0,\, -5,\, -20]^T$ m, and $\boldsymbol{v}_1(0) = \boldsymbol{v}_2(0) = [0,\, 0,\, 0]^T$ m/s at $t_0 = 0$ s, with the payload at rest. The initial attitude is represented by $\boldsymbol{\eta}_1(0) = -\boldsymbol{\eta}_2(0) = [0.1462,\, 0,\, 0]$ rad, while the desired yaw angle is $\psi_{sp_1} = \psi_{sp_2} = 0$ rad. The first simulation case consists in performing a hover–to–hover delivery maneuver, with an intermediate ten seconds stop, under disturbances and actuator fault, with an imposed overall maneuver time $t_m = 50$ s. In particular, a constant wind $w = [0, -10, 0]^T$ m/s perturbs the system during the time interval $5.5 \leq t \leq 8.5$ s, thus simulating a discrete gust. In the second part of the maneuver, atmospheric turbulence is introduced to disturb the state of both the octarotor and the payload. The turbulence is modeled using a dedicated Simulink Aerospace Blockset component, which implements the Von Kàrmàn spectral representation. The approach is grounded in the mathematical formulations provided by the Military Specification MIL-F-8785C and the Military Handbook MIL–HDBK–1797B, referenced in Refs. 33 and 34, respectively. The following parameters are set:

- specification: MIL–F–8785C;

- model type: continuous Von Kàrmàn (+q +r);
- wind speed at 6 m (used to define the low–altitude wind intensity): 5 m/s;
- wind direction at 6 m (degrees clockwise from North): 90 deg;
- scale length at medium/high altitudes: 533.4 m (default);
- band–limited noise sample time: 0.002 s;
- MR wingspan: 2.38 m (maximum octarotor frontal size);
- load wingspan: 1 m (maximum load frontal size);

Moreover, for $t \geq 28$ s, Agent 1 experiences a malfunctioning of propeller 2 caused by an abrupt and persistent 15% rotational speed loss. The reference trajectory $\boldsymbol{r}_r(t)$ is a C^1 cubic polynomial of the following form

$$\boldsymbol{r}_r(t) = \begin{cases} [-0.089\, t^3 + 0.2\, t^2, 0, -20]^T & 0 < t \leq 15\, s \\ [15, 0, -20]^T & 15 < t \leq 25\, s \\ [-0.0119\, \tau^3 + 0.267\, \tau^2 + 15, 0, -20]^T & 25 < t \leq 40\, s \end{cases} \tag{49}$$

where $\tau = t - 25$. A comparison is made between the sub–case with baseline formation control only and the sub–case where $\mathcal{L}_1$ AC is added to the control action. In Fig. 5, the East positions of the three objects are reported with respect to time. The additive $\mathcal{L}_1$ contribution provides high robustness against both the wind gust in the first part of the maneuver and the actuator fault in the second one. The agents, after being perturbed, show a very fast reaction in re–gaining the desired formation geometry. Similar considerations hold for Fig. 6, where the vertical positions of the three objects are depicted. Here the main concern is the altitude drop caused by the partial loss of a propeller of Agent 1. The augmented layer immediately accounts for the failure and stabilizes the system without significantly losing height, while the baseline controller lacks of robustness leading to height loss even once the desired position is reached. Finally, Fig. 7 reports the position and velocity errors, respectively. While the velocity error $\boldsymbol{e}_v$ remains almost unaltered, the position error $\boldsymbol{e}_p$ is significantly smaller, thanks to the beneficial contribution provided by the $\mathcal{L}_1$ augmentation. In this regard, performance indicators obtained through the two different control layers are detailed in Table 1. For the same maneuver time, there is a slight improvement in the propulsive energy reduction, which can be considered negligible. However, the other indicators are notably improved, demonstrating the favorable contribution of the proposed method.

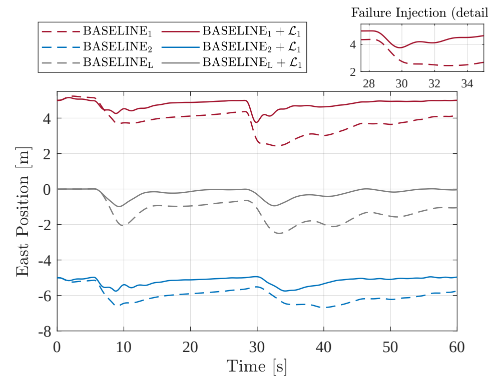

Figure 5: Multirotors and load East position with and without $\mathcal{L}_1$ AC (test case 1).

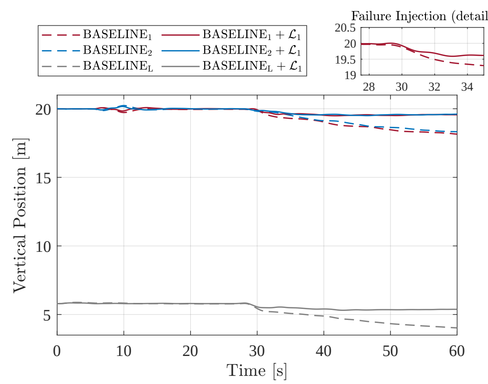

Figure 6: Multirotors and load vertical position with and without $\mathcal{L}_1$ AC (test case 1).

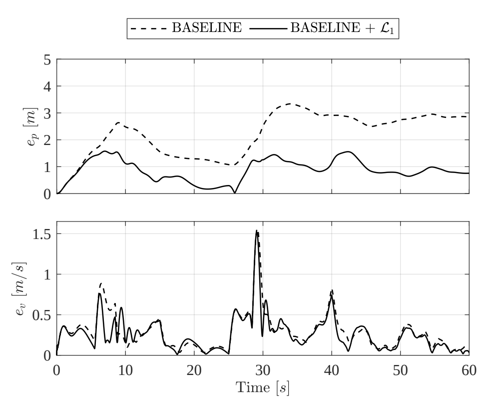

Figure 7: Position and velocity errors with and without $\mathcal{L}_1$ AC (test case 1).

Table 1: Relevant performance indicators (test case 1).

Index	BASELINE	BASELINE + $\mathcal{L}_1$
$\boldsymbol{e}_{p_{av}}$ [m]	2.20	0.87 (-50.45%)
$\boldsymbol{e}_{v_{av}}$ [m/s]	0.29	0.26 (-10.01%)
$\boldsymbol{e}_{p_{max}}$ [m]	3.34	1.58 (-52.76%)
$\boldsymbol{e}_{p_{max}}$ [m/s]	1.56	1.52 (-2.91%)
E_{prop} [Wh]	564.90	557.97 (-1.29%)

4.3.2. Test case 2

In this case, the formation is required to track a sequence of seven waypoints $\boldsymbol{WP}_i = [x_i, y_i, z_i]^T$, $i = 1, \ldots, 7$. Following from the formulation of Section 3.2, the i–th vehicle's desired position is based on the reference point trajectory and is given by $\bar{\boldsymbol{r}}_i = \boldsymbol{r}_r + \bar{\boldsymbol{d}}_i$. Without loss of generality, a waypoint is considered to be reached when the positioning error of Agent 1, defined as $\varepsilon_P = \|\boldsymbol{WP}_i - \boldsymbol{r}_1\|$, remains below 0.5 m for at least 5 s. This simulation scenario envisages a sample urban parcel–delivery mission. Starting from a nominal hover condition, the formation immediately moves to a first pick–up location ($\boldsymbol{WP}_1$) and then visits five drop–off sites before ending the operation when returning to the initial hovering position ($\boldsymbol{WP}_7$). Abrupt payload–mass changes at selected waypoints (see Table 2) model loading and unloading events. Controller performance with and without $\mathcal{L}_1$ AC are evaluated under the same load mass variation disturbances.

In Fig. 8, the trajectory followed by Agent 1 is reported. It is evident that, when load mass is increased by 50% ($\boldsymbol{WP}_1$), the baseline controller lacks sufficient robustness, resulting in a vertical deviation of several meters and reducing the accuracy of trajectory tracking. The augmented control system shows improved robustness and fast adaptation against non–nominal conditions, allowing to fulfill the delivery tasks more smoothly. In this respect, maneuver time with the $\mathcal{L}_1$ adaptive layer active is reduced from 143.89 s to 126.96 s, allowing for a concurrent decrease of power consumption (see Table 3).

Position error $\boldsymbol{e}_p$ is depicted in Fig. 9, while Table 3 details significant reduction in both the average and the maximum position errors (more than 30 % and 7 %, respectively).

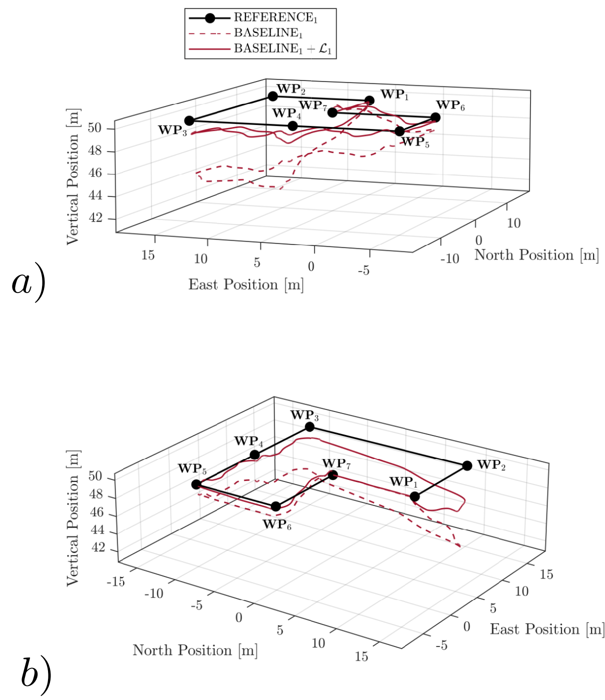

Figure 8: Waypoint–based 3D trajectory followed by Agent 1 with and without $\mathcal{L}_1$ AC from the different camera views a) and b) (test case 2).

Table 2: Waypoints of the delivery mission (test case 2).

i–th waypoint	x_i [m]	y_i [m]	z_i [m]	m_l [kg]
1	10	0	-50	150
2	10	-10	-50	125
3	-10	10	-50	115
4	-10	0	-50	105
5	-10	-10	-50	105
6	0	-10	-50	95
7	0	0	-50	95

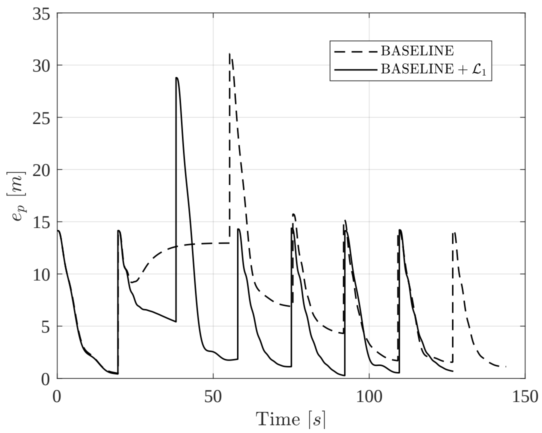

Figure 9: Position error with and without $\mathcal{L}_1$ AC (test case 2).

Table 3: Relevant performance indicators (test case 2).

Index	BASELINE	BASELINE + $\mathcal{L}_1$
t_m [s]	143.89	126.96 (-11.77%)
$\boldsymbol{e}_{p_{av}}$ [m]	7.88	5.42 (-31.20%)
$\boldsymbol{e}_{p_{max}}$ [m]	31.11	28.80 (-7.44%)
E_{prop} [Wh]	1245.10	1116.60 (-10.32%)

5. CONCLUSIONS

This study proposed a cooperative $\mathcal{L}_1$ adaptive augmentation strategy for a baseline formation controller, aiming to achieve rapid adaptation while ensuring robustness against external disturbances. By leveraging the inherent decoupling in the dynamics of cooperative slung–load systems, the adaptive control loops were independently designed and tuned for the forward–swing and lateral–vertical channels. For the forward–swing channel, global exponential ultimate boundedness was formally established. Although initially developed for a nominal formation of three point masses, the controller was evaluated through high–fidelity simulations that replicated sample Urban Air Mobility and Delivery scenarios. These simulations incorporated the nonlinear dynamics of two octarotor UAVs, viscoelastic cable effects, both matched and unmatched model uncertainties, sensor noise, and external disturbances. In all test cases, the $\mathcal{L}_1$–augmented controller consistently outperformed the baseline, demonstrating improved tracking accuracy and greater energy efficiency. Moreover, the proposed approach remains compatible with standard flight control hardware and readily generalizable to a variety of rotorcraft configurations with minimal modification.

Appendix A. Proof of Theorem 1

Consider the forward-swing state prediction error

$$\tilde{\boldsymbol{x}} = \hat{\boldsymbol{x}}_{fs} - \boldsymbol{x}_{fs} \in \mathbb{R}^6 \tag{A.1}$$

and the parameter estimation error

$$\tilde{\boldsymbol{\sigma}} = \begin{bmatrix} \tilde{\boldsymbol{\sigma}}_1 \\ \tilde{\boldsymbol{\sigma}}_2 \end{bmatrix} = \begin{bmatrix} \hat{\boldsymbol{\sigma}}_{1_{fs}} - \boldsymbol{f}_{1_{fs}} \\ \hat{\boldsymbol{\sigma}}_{2_{fs}} - \boldsymbol{f}_{2_{fs}} \end{bmatrix} \in \mathbb{R}^6 \tag{A.2}$$

Note that there exist constants $\boldsymbol{\Delta}_1$, $\boldsymbol{\Delta}_2$ such that the parameter estimation error is bounded. In the open interval $t \in [k\,T_s,\,(k+1)\,T_s)$, between two sampling instants, the error dynamics is

$$\dot{\tilde{\boldsymbol{x}}} = \boldsymbol{A}_m\,\tilde{\boldsymbol{x}} + \boldsymbol{B}_m\,(\tilde{\boldsymbol{\omega}}\boldsymbol{u} + \tilde{\boldsymbol{\sigma}}_1) + \boldsymbol{B}_{um}\,\tilde{\boldsymbol{\sigma}}_2 \tag{A.3}$$

where $\boldsymbol{A}_m := \boldsymbol{A}_{m_{fs}}$, $\boldsymbol{B}_m := \boldsymbol{B}_{m_{fs}}$, $\tilde{\boldsymbol{\omega}} := \boldsymbol{\omega}_{fs} - \boldsymbol{\omega}_0$, $\boldsymbol{u} := \boldsymbol{u}_{fs}$, and $\boldsymbol{B}_{um} := \boldsymbol{B}_{um_{fs}}$. Let the gain–mismatch term be $\boldsymbol{d} := \tilde{\boldsymbol{\omega}}\,\boldsymbol{u}$ and bounded, namely $\|\boldsymbol{d}\| \leq \boldsymbol{\Delta}_\omega$. Let one pick the following Lyapunov candidate function

$$V(t) = \tilde{\boldsymbol{x}}^T\,\boldsymbol{P}\,\tilde{\boldsymbol{x}} + \tilde{\boldsymbol{\sigma}}^T\,\boldsymbol{\Lambda}^{-1}\,\tilde{\boldsymbol{\sigma}} \tag{A.4}$$

where $\boldsymbol{P}$ is the solution of the Lyapunov matrix equation $\boldsymbol{A}_{m_{fs}}^T\,\boldsymbol{P} + \boldsymbol{P}\,\boldsymbol{A}_{m_{fs}} = -\boldsymbol{Q}$ and $\boldsymbol{\Lambda}$ is a symmetric, positive–definite adaptation gain matrix. By taking the time derivative of Eq. (A.4) on an open interval and plugging in Eq. (A.3), one obtains

$$\dot{V}(t) = -\tilde{\boldsymbol{x}}^T\boldsymbol{Q}\tilde{\boldsymbol{x}} + 2\tilde{\boldsymbol{x}}^T\boldsymbol{P}\boldsymbol{B}_m\tilde{\boldsymbol{\eta}}_1 + 2\tilde{\boldsymbol{x}}^T\boldsymbol{P}\boldsymbol{B}_{um}\tilde{\boldsymbol{\eta}}_2 \tag{A.5}$$

where $\tilde{\boldsymbol{\eta}}_1 := \boldsymbol{d} + \tilde{\boldsymbol{\sigma}}_1$ and $\tilde{\boldsymbol{\eta}}_2 := \tilde{\boldsymbol{\sigma}}_2$ By taking into account the Young inequality

$$2\boldsymbol{a}^T\boldsymbol{b} \leq \epsilon\|\boldsymbol{a}\|^2 + \frac{1}{\epsilon}\|\boldsymbol{b}\|^2 \tag{A.6}$$

it is possible to derive eigen–bounds for both the matched and unmatched parts. In particular, it is

$$\|\tilde{\boldsymbol{x}}\|^2 \leq \frac{1}{\lambda_{min}(\boldsymbol{P})} V \tag{A.7}$$

$$\begin{aligned} \|\tilde{\boldsymbol{\eta}}_1\|^2 &\leq \lambda_{max}(\boldsymbol{\Lambda}) V + (\boldsymbol{\Delta}_1 + \boldsymbol{\Delta}_\omega)^2 \\ &\leq \lambda_{max}(\boldsymbol{\Lambda}) V + \bar{\boldsymbol{\Delta}}_1^2 \end{aligned} \tag{A.8}$$

$$\|\tilde{\boldsymbol{\eta}}_2\|^2 \leq \lambda_{max}(\boldsymbol{\Lambda}) V + \boldsymbol{\Delta}_2^2 \tag{A.9}$$

where $\bar{\boldsymbol{\Delta}}_1 = \boldsymbol{\Delta}_1 + \boldsymbol{\Delta}_\omega$. By applying the Young inequality with $\epsilon = \lambda_{min}(Q)/4$ and introducing the above eigen–bounds, one obtains the following ordinary differential inequality

$$\dot{V}(t) \leq \xi V(t) + d_0 \tag{A.10}$$

where

$$\xi = -\tfrac{\lambda_{min}(\boldsymbol{Q})}{2\lambda_{min}(\boldsymbol{P})} + \tfrac{4\lambda_{max}(\boldsymbol{\Lambda})}{\lambda_{min}(\boldsymbol{Q})} \left(\|\boldsymbol{PB}_m\|^2 + \|\boldsymbol{PB}_{um}\|^2\right) \tag{A.11}$$

and

$$d_0 = \tfrac{4}{\lambda_{min}(\boldsymbol{Q})} \left(\|\boldsymbol{PB}_m\|^2 \|\bar{\boldsymbol{\Delta}}_1\|^2 + \|\boldsymbol{PB}_{um}\|^2 \|\boldsymbol{\Delta}_2\|^2\right). \tag{A.12}$$

Remark 4. Note that the exponential decay of the homogeneous part of Eq. (A.10) is guaranteed by picking $\boldsymbol{\Lambda}$ such that $\xi < 0$. A sufficient condition, obtained directly from (A.11), can be

$$\lambda_{\max}(\boldsymbol{\Lambda}) < \frac{\lambda_{\min}^2(\boldsymbol{Q})}{8\,\lambda_{\min}(\boldsymbol{P})\left(\|\boldsymbol{PB}_m\|^2 + \|\boldsymbol{PB}_{um}\|^2\right)}. \tag{A.13}$$

Since $\boldsymbol{\Lambda}$ is a design parameter, the requirement can be always fulfilled with a proper choice of this adaptation gain matrix.

The solution of Eq. (A.10) is obtained from the corresponding linear, first-order ordinary differential equation with initial condition $V(t_0) = V_0 \geq 0$ as

$$V(t) \leq (1-\beta)\, V_0 + \frac{d_0\, \beta}{|\xi|} \tag{A.14}$$

where $\beta := 1 - e^{\xi\, T_s} \in (0,\, 1)$. By choosing $T_s > 0$ such that $||e^{\boldsymbol{A}_{m_{fs}} T_s}|| \leq 1-\alpha$ and applying it to Eq. (A.14) at the sampling instant $t_{k+1} = (k+1)\, T_s$, one has

$$V(t_{k+1}) \leq (1-\alpha)\, V(t_{k+1}^-), \tag{A.15}$$

where t_{k+1}^- is the value right before the update and α introduces a contraction factor between two consecutive samples. The combination of Eq. (A.10) and (A.15) yields an expression for the generic $k+1$ time step as $V_{k+1} \leq \rho\, V_k + q$ where $V_{k+1} := V\left((k+1)\, T_s\right)$, $V_k := V(k\, T_s)$, $\rho := (1-\alpha)(1-\beta)$, and $q := (1-\alpha)\beta \frac{d_0}{|\xi|}$. By definition $0 < \rho < 1$, thus the classical geometric–series argument gives

$$\begin{aligned} V_k \leq \rho^k\, V_0 + \frac{q}{1-\rho} &= \rho^k\, V_0 + \frac{(1-\alpha)\beta}{1-\rho} \frac{d_0}{|\xi|} \\ &= \rho^k\, V_0 + V_\infty \end{aligned} \tag{A.16}$$

where

$$V_\infty = \frac{(1-\alpha)\beta}{1-\rho} \frac{d_0}{|\xi|}. \tag{A.17}$$

Since the closed-loop map from $\tilde{\boldsymbol{\sigma}}$ to the output error $\boldsymbol{e}_{fs}$ is exactly $\boldsymbol{e}_{fs} = C(s)\tilde{\boldsymbol{\sigma}}$, and $C(s)$ is strictly proper and stable, its $\mathcal{L}_1$ induced gain is finite. Then, for every $t \geq 0$, the convolution inequality yields

$$\|\boldsymbol{e}_{fs}\|_\infty \leq g_e \sup_{0 \leq \tau \leq t} \|\tilde{\boldsymbol{\sigma}}(\tau)\|. \tag{A.18}$$

From the Lyapunov analysis it is possible to derive the uniform–ultimate bound

$$\sup_{t \geq 0} \|\tilde{\boldsymbol{\sigma}}(\tau)\| \leq \sqrt{\lambda_{max}(\boldsymbol{\Lambda})\, V_\infty}, \tag{A.19}$$

with V_∞ already defined in Eq. (A.16). By combining Eq. (A.18) and (A.19), one finally obtains

$$\|\boldsymbol{e}_{fs}(t)\|_\infty \leq g_e \sqrt{\lambda_{\max}(\boldsymbol{\Lambda})\, V_\infty} \qquad \forall t \geq 0, \tag{A.20}$$

which coincides exactly with the performance bound stated in Theorem 1. □

Appendix B. Slung–load system parameters

The most relevant system parameters are summarized in Table B.1 below.

Table B.1: Multirotor slung–load system parameters

Parameter	Symbol	Value	Units
Multirotor			
Mass	m	70	kg
Center of gravity position	$STA_P = BL_P$	0	m
	WL_P	-0.15	m
Moments of inertia	J_{11}	10.61	$\mathrm{kg\,m^2}$
	J_{22}	10.31	$\mathrm{kg\,m^2}$
	J_{33}	19.74	$\mathrm{kg\,m^2}$
	J_{12}	0.037	$\mathrm{kg\,m^2}$
	J_{13}	-0.043	$\mathrm{kg\,m^2}$
	J_{23}	-0.003	$\mathrm{kg\,m^2}$
Center of pressure position	$STA_{CP} = BL_{CP}$	0	m
	WL_{CP}	-0.125	m
Frame drag areas	$A_1 = A_2$	0.22	$\mathrm{m^2}$
	A_3	1.03	$\mathrm{m^2}$
Propeller			
Number of blades	n_b	2	
Radius	R	0.5	m
Mean aerodynamic chord	$\bar{c}$	0.086	m
Chord @ 75% R	c_{75}	0.103	m
Lift curve slope	a	5.9	$\mathrm{rad^{-1}}$
Pre–cone angle	a_0	0	rad
Root pitch angle	θ_0	0.7854	rad
Total twist	θ_t	-0.6981	rad
Load			
Mass	m_l	100	kg
Reference area	A_l	0.785	$\mathrm{m^2}$
Drag coefficient (sphere)	C_{dl}	0.5	
Cable			
Nominal length	L	15	m
Hooke's constant	K	90 950	$\mathrm{N\,m^{-1}}$
Damping coefficient	C	215	$\mathrm{N\,m^{-1}\,s}$
Hook point position	$STA_H = BL_H$	0	m
	WL_H	-0.2	m

6. ACKNOWLEDGMENTS

This study was carried out within the MOST—Sustainable Mobility National Research Center and received funding from the European Union Next–GenerationEU (PIANO NAZIONALE DI RIPRESA E RESILIENZA (PNRR) – MISSIONE 4 COMPONENTE 2, INVESTIMENTO 1.4 – D.D. 1033 17/06/2022, CN00000023). This manuscript reflects only the authors' views and opinions, neither the European Union nor the European Commission can be considered responsible for them.

References

[1] Biehle, T., "Social Sustainable Urban Air Mobility in Europe," *Sustainability*, 14(15), 2022, 9312, DOI: https://DOI.org/10.3390/su14159312.

[2] Dalpadulo, E., Vergnano, A., Leali, F., "Urban Air Mobility for Medical Delivery: An Innovative Approach to Healthcare Logistics," In: Di Stefano, P., Gherardini, F., Nigrelli, V., Rizzi, C., Sequenzia, G., Tumino, D. (eds) *Design Tools and Methods in Industrial Engineering IV. ADM 2024. Lecture Notes in Mechanical Engineering. Springer*, Cham., DOI: https://doi.org/10.1007/978-3-031-76597-1.

[3] Hewett, R., Puangpontip, S., "On Controlling Drones for Disaster Relief," *Procedia Computer Science*, 207, 2022, pp. 3703–3712, DOI: https://DOI.org/10.1016/J.PROCS.2022.09.430.

[4] Valente, M., del Prete, C., Facci, G., Martino, A., Grilli, G. R., Bravi, F., Reno, C., Ragazzoni, L., "The 2023 floods in the Emilia-Romagna Region, Italy: A retrospective qualitative investigation into response strategies and criticalities," *International Journal of Disaster Risk Reduction*, 116, 2025 105089, DOI: https://DOI.org/10.1016/J.IJDRR.2024.105089.

[5] Estevez, J., Garate, G., Lopez-Guede, J. M., Larrea, M., "Review of Aerial Transportation of Suspended-Cable Payloads with

Quadrotors," *Drones*, 8(35), 2024, pp. 1–21, DOI: https://DOI.org/10.3390/drones8020035.

[6] Pounds, P. E. I., Bersak, D. R., Dollar, A. M., "Grasping From the Air: Hovering Capture and Load Stability," in: *Proc. of IEEE Int. Conf. Robot. Autom.*, 2011, pp. 2491–2498, DOI: https://DOI.org/10.1109/ICRA.2011.5980314.

[7] Chen, H., Quan, F., Fang, L., Zhang, S., "Aerial Grasping with a Lightweight Manipulator Based on Multi-Objective Optimization and Visual Compensation," *Sensors*, 19, 2019, 4253, DOI: https://DOI.org/10.3390/s19194253.

[8] Eskandaripour, H., Boldsaikhan, E., "Last-Mile Drone Delivery: Past, Present, and Future," *Drones*, 7(2), 2023, pp. 1–19, DOI: https://DOI.org/10.3390/drones7020077.

[9] Li, X., Zhang, J., Han, J., "Trajectory planning of load transportation with multi-quadrotors based on reinforcement learning algorithm," *Aerosp. Sci. Technol.*, 116, 2021, 106887, DOI: https://DOI.org/10.1016/j.ast.2021.106887.

[10] de Angelis, E. L., Giulietti, F., "Stability and control issues of multirotor suspended load transportation: An analytical closed-form approach," *Aerosp. Sci. Technol.*, 135, 2023, 108201, DOI: https://DOI.org/10.1016/j.ast.2023.108201.

[11] Cao, C., Hovakimyan, N., "Design and Analysis of a Novel $\mathcal{L}_1$ Adaptive Controller, Part I: Control Signal and Asymptotic Stability," in *Proceedings of the 2006 American Control Conference*, Minneapolis, MN, USA, 2006, pp. 3397–3402, DOI: https://DOI.org/10.1109/ACC.2006.1657243.

[12] Cao, C., Hovakimyan, N., "Stability Margins of $\mathcal{L}_1$ Adaptive Controller: Part II," in *Proceedings of the 2007 American Control Conference*, New York, NY, USA, 2007, pp. 3931–3936, DOI: https://DOI.org/10.1109/ACC.2007.4282486.

[13] Cao, C., Hovakimyan, N., "$\mathcal{L}_1$ adaptive controller for systems with unknown time-varying parameters and disturbances in the presence of non-zero trajectory initialization error," *International Journal of Control*, 81(7), 2008, pp. 1147–1161, DOI: https://DOI.org/10.1080/00207170701670939.

[14] Xargay, E., Hovakimyan, N., Cao, C., "$\mathcal{L}_1$ adaptive controller for multi-input multi-output systems in the presence of nonlinear unmatched uncertainties," in *Proceedings of the 2010 American Control Conference*, Baltimore, MD, USA, 2010, pp. 874–879, DOI: https://DOI.org/10.1109/ACC.2010.5530686.

[15] Bichlmeier, M., Holzapfel, F., Xargay, E., Hovakimyan, N., "$\mathcal{L}_1$ Adaptive Augmentation of a Helicopter Baseline Controller," in *Proceedings of the 2013 AIAA Guidance, Navigation, and Control (GNC) Conference*, Boston, Massachusetts, USA, August 2013, DOI: https://DOI.org/10.2514/6.2013-4855.

[16] Bullock, J., Trujillo, A., Cheng, S., Hovakimyan, N., "Robust Path-Following Controller for Multirotor Vehicles in Uncertain Wind Conditions," in *Proceedings of AIAA SCITECH 2025 Forum*, Orlando, FL, USA, January 2025, DOI: https://DOI.org/10.2514/6.2025-1121.

[17] Suárez Fernández, R. A., Dominguez, S., Campoy, P., "$\mathcal{L}_1$ adaptive control for Wind gust rejection in quad-rotor UAV wind turbine inspection," in *Proceedings of 2017 International Conference on Unmanned Aircraft Systems (ICUAS)*, Miami, FL, USA, 2017, pp. 1840–1849, DOI: https://DOI.org/10.1109/ICUAS.2017.7991485.

[18] Costantini, E., de Angelis, E. L., Giulietti, F., "Cooperative Drone Transportation of a Cable-Suspended Load: Dynamics and Control," *Drones*, 8(9), 2024, 434, DOI: https://DOI.org/10.3390/drones8090434.

[19] de Angelis, E. L., Giulietti, F., Rossetti, G., "Multirotor aircraft formation flight control with collision avoidance capability," *Aerosp. Sci. Technol.*, 77, 2018, pp. 733–741, DOI: https://DOI.org/10.1016/j.ast.2018.04.002.

[20] de Angelis, E. L., "Swing angle estimation for multicopter slung load applications," *Aerosp. Sci. Technol.*, 89, 2019, pp. 264–274, DOI: https://DOI.org/10.1016/j.ast.2019.04.014.

[21] de Angelis, E. L., Giulietti, F., "An Improved Method for Swing State Estimation in Multirotor Slung Load Applications," *Drones*, 7(11), 2023, 654, DOI: https://DOI.org/10.3390/drones7110654.

[22] Costantini, E., de Angelis, E. L., Giulietti, F., "Cooperative Transportation Using Rotorcraft: Swing State Estimation and Control," in *Proc. of 50th European Rotorcraft Forum*, Marseille, France, 2024, pp. 1–14.

[23] PX4 Development Team and Community, PX4 Autopilot User Guide (main), <https://docs.px4.io/main/en/>.

[24] Talbot, P. D., Tinling, B. E., Decker, W. A., Chen, R. T. N., "A mathematical Model for a Single Main Rotor Helicopter for Piloted Simulation," NASA TM 84281, 1982.

[25] Leishman, J. G., *Principles of Helicopter Aerodynamics*, 2nd edition, Cambridge University Press, New York, 2006, Chapters 2 and 5.

[26] Padfield, G. D., *Helicopter Flight Dynamics*, 2nd edition, Blackwell Pub., Oxford, 2007, Chapter 3.

[27] de Ruiter, A. H. J., Damaren, C. J., Forbes, J. R., *Spacecraft Dynamics and Control - An Introduction,* John Wiley & Sons, Ltd., Sussex, 2013, Chapters 19–24.

[28] Hovakimyan, N., Cao, C., *L1 Adaptive Control Theory: Guaranteed Robustness with Fast Adaptation (Advances in Design and Control,*, Society for Industrial and Applied Mathematics (SIAM), 3600 Market Street, Philadelphia, (2010), Chapter 3.

[29] Butcher, J. C., "Numerical methods for ordinary differential equations in the 20th century," *J. Comput. Appl. Math.*, 125, (2000), pp. 1–29, DOI: https://doi.org/10.1016/S0377-0427(00)00455-6.

[30] Costantini, E., de Angelis, E. L., Giulietti, F., "Cooperative Transportation of a Cable–Suspended Load Using Rotorcraft: A Minimal Swing Approach," in: *Proc. of 49th European Rotorcraft Forum*, Bückeburg, Germany, 2023, 1–14.

[31] U.S. Government Printing Office, "U.S. Standard Atmosphere," NOAA-S/T 76-1562, (1976), pp. 1–241.

[32] Defense Mapping Agency Washington DC, *Department of Defense World Geodetic System 1984: Its Definition and Relationships with Local Geodetic Systems,* 2nd edition, (1991), pp. 1–170.

[33] U.S. Department of Defense, *Flying Qualities of Piloted Airplanes*, U.S. Military Specification MIL–F–8785C, 1980, 1–95.

[34] U.S. Department of Defense, *Flying Qualities of Piloted Aircraft*, U.S. Military Handbook MIL–HDBK–1797B, 2012, 1–849.